Spatial evolution of a film flowing down a fiber

C. Duprat, C. Ruyer-Quil, and F. Giorgiutti-Dauphiné
Laboratory FAST, Université Pierre et Marie Curie and Université Paris-Sud, CNRS, Batiment 502, Campus Univ., Orsay 91405, France

(Received 17 December 2008; accepted 20 March 2009; published online 27 April 2009)

We report the response to a forcing at the inlet of a film flowing down a vertical fiber. Parameters are chosen in order to examine the effects of both inertia and surface tension. The spatial response of the film to inlet forcing depends on the ratio of the forcing frequency f_{for} to the frequency f_M corresponding to the maximum linear growth rate. At $f_{\text{for}} \approx f_M$, the primary instability leads directly to the formation of a saturated wavetrain at the forcing frequency, whereas at low forcing frequencies $f_{\text{for}} < f_M$, this formation is preceded by a sequence of periodic coalescence events. The amplitude, speed, profiles, and inner flow pattern of traveling waves have been characterized and compared to the solutions to the two-equation model obtained by Ruyer-Quil *et al.* [J. Fluid Mech. **603**, 431 (2008)], showing a remarkable agreement. A steepening of the waves is observed when inertia becomes dominant. An excellent correlation between data is observed when the amplitude and speed of the waves are made dimensionless with reference to the substrate thickness and free-surface velocity. © *2009 American Institute of Physics*. [DOI: 10.1063/1.3119811]

I. INTRODUCTION

A thin liquid film flowing down a vertical fiber is always unstable and exhibits fascinating dynamical regimes. Such flows are of widespread practical importance, for example, in industrial processes such as optical fiber coating. Under the action of surface tension, viscous diffusion, and inertia, the resulting flow evidences various wavy regimes including droplike regimes, solitary waves, secondary instabilities, or complex disordered patterns. Such a complexity arises from the interplay of two different instability mechanisms. The first one is the Rayleigh–Plateau instability of a fluid cylinder prompted by capillarity, whereas the second one is the hydrodynamic instability of a falling film prompted by inertia, referred hereinafter as the Kapitza mode of instability.[1,2]

The first experimental investigation of flows down fibers was made by Quéré in the context of drawing of wires from liquid baths.[3,4] Quéré observed the formation of axisymmetric drops and showed that this break-up process may be arrested by the mean flow advection. Flow rates were very small due to the experimental procedure. By regularly wetting the fiber from the top, Kliakhandler *et al.*[5] and Craster and Matar[6] considered the instability of a uniform film at larger flow rates and reported the nonlinear dynamics of the axisymmetric waves or beads far from the inlet.

In a previous paper,[7] we reported experimental data on the onset of the primary instability close to the inlet. Two different situations were observed whether or not the primary wavetrain was regular or irregular. In the former case we showed that the base flow was absolutely unstable and the primary flow exhibited its own intrinsic dynamics with a well-defined frequency, whereas in the latter case the base flow was convectively unstable and selectively amplified inlet perturbations. The absolutely unstable situation was observed only when the Rayleigh–Plateau instability was dominant and at low flow rates and small fiber radii. When inertia effects were important and thus the Kapitza mode was dominant, i.e., at large flow rate or at large fiber radii, the uniform film was always found to be convectively unstable. Accordingly, inertia was shown to displace the transition from a convective to an absolute instability in favor to the convective situation.

In the present paper we experimentally document the spatial response of the convectively unstable flow at moderate Reynolds number when the system behaves as a noise amplifier and the Kapitza mode of instability competes with the Rayleigh–Plateau instability. To our knowledge, no experimental data are available for this case, the experiments by Quéré and Kliakhandler *et al.* considering only very viscous fluids for which inertia is negligible. The emphasis is put on the characteristics (speed, amplitude, shape, and inner velocity distribution) of the nonlinear periodic waves propagating at constant speed and with a constant shape, i.e., *traveling waves*, that dominate the flow dynamics at the bottom of the fiber. We thus complete our previous work[7] that focused on the linear inception region at the top of the fiber. A secondary aim of this study is to extend the validation of the weighted residual modeling approach developed in Ref. 8 up to moderate Reynolds numbers.

In Sec. II, the experimental setup is briefly described and a first qualitative description of the wavy regimes is presented. In Sec. III, we recall the main steps leading to the formulation of a two-equation model detailed in Ref. 8. In Sec. IV, we present experimental results in the case of naturally excited flows in the upper part of the fiber and compare with the linear primary instability analysis. We then study in Sec. V the response of the film to periodic perturbations at the inlet. Finally, quantitative characteristics of the solitary waves are presented and compared to the numerical results to the model. Lastly, the shape of the waves provides information on the dominant instability mode: Rayleigh–Plateau or Kapitza mode.

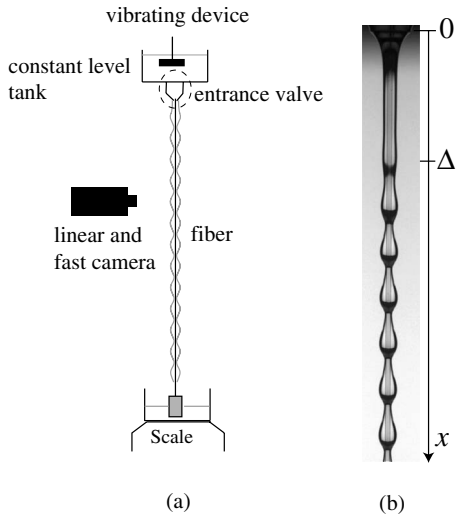

FIG. 1. (a) Experimental setup. (b) A view of the liquid film at the top of the fiber. △ refers to the healing length.

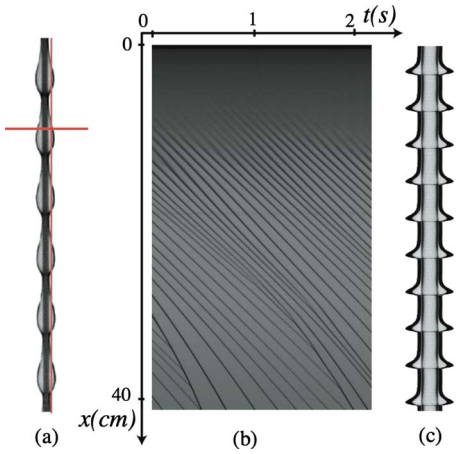

FIG. 3. (Color online) (a) Two positions of the pixel line of the linear camera. (b) Spatiotemporal diagram achieved with a vertical pixel line. (c) Thickness fluctuations in time at a given height for a horizontal pixel line.

II. EXPERIMENTAL PROCEDURE AND FLOW REGIMES

A. Experimental setup

In the present work, we study the flow of Rhodorsil silicon oil v50 (density $\rho=963$ kg/m^3, kinematic viscosity $\nu=50$ mm^2/s, and surface tension $\gamma=20.8$ mN/m at 25 °C) and v100 ($\rho=965$ kg/m^3, $\nu=100$ mm^2/s, and $\gamma=20.9$ mN/m at 25 °C) on a 1.5 m long Nylon fishing thread of various radii R with $0.2<R<1.5$ mm. The experimental setup is presented in Fig. 1(a). The fluid is supplied by an entrance valve which is detailed in Fig. 2. It consists of two cone-shaped parts: The upper part 1 is fixed on the tank. The lower part 2 is screwed on 1. The fluid is then guided on the fiber through gap 3 between the cones. We can thus control the entrance flow rate by varying gap 3. The axisymmetry of the base flow is ensured by means of the two adjusting screws 4 and the pivot 5. The horizontality of part 1 is also adjusted by this system. Such a design limits the entrance noise so that thickness fluctuations are of the order of 10^{-3}%.

The fluid level in the tank is maintained constant (to ensure a constant flow rate) and the end of the fiber is attached to a weight to guarantee its verticality. The mass flow rate Q_m is measured with computer-controlled scales placed below the collecting tank.

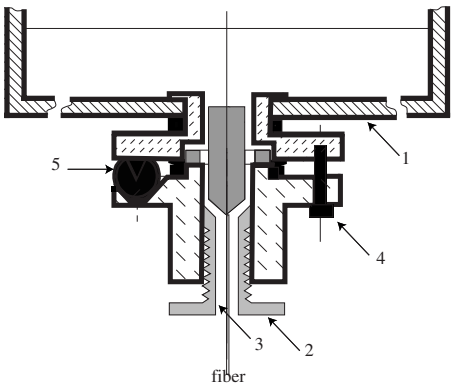

FIG. 2. Design of the entrance valve.

The determination of the various characteristics of the flow is achieved by means of spatiotemporal diagrams: a vertical line (selected passing through the drops) of a linear camera is recorded and stored at constant time intervals which reveals the (x,t) trajectories of the patterns [Figs. 3(a) and 3(b)]. Parallel striations reflect the motion of constant height structures (drops or waves). Another possible orientation of the pixel line is perpendicularly to the flow. This configuration then allows to detect fluctuations of the film thickness with time at a position on the fiber with great sensitivity [Fig. 3(c)]. The shapes of the structures are finally captured by a fast digital camera. To study the response of the system to periodic perturbations, a vibrating device produces periodic pressure perturbations just above the entrance valve in the tank. The frequency and the amplitude of the perturbations can be adjusted. We obtain forcing frequencies f_{for} ranging from 0.1 to 50 Hz.

In the given experiments, we confined ourselves to a study of three different fiber radii ($R=1.5$, 0.475, and 0.2 mm) with a possible range of flow rate corresponding to a range of uniform film thickness h_N at the inlet $0.6R<h_N<5R$.

B. Experimental observations of the "natural" dynamics

Depending on the flow rate and the fiber radius, two distinct scenarios are observable for the spatial evolution of the film down the fiber.[7] At small flow rates or for thin fibers, the observed wave pattern is very regular and extends from the top to the bottom of the fiber without noticeable variations. The system then behaves like a self-sustained oscillator selecting its own well-defined frequency. At larger flow rates or for thicker fibers, the dynamics becomes irregular and the flow behaves as a noise amplifier, thus responding to inlet perturbations. We showed[7] that the transition from a

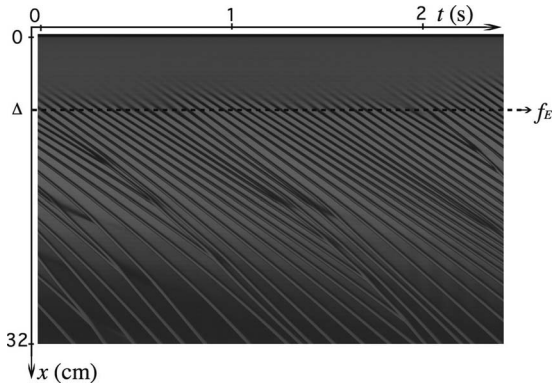

FIG. 4. Natural spatiotemporal evolution (no forcing) of the film at the top of the fiber ($0<x<32$ cm) for $R=0.475$ mm and $h_N=0.78$ mm ($R/l_c=0.32$ and $\tilde{\alpha}=1.64$).

regular wave pattern to an irregular one corresponds to the transition between an absolute to a convective instability.

In the convective regime, perturbations at the entrance of the system (noise or controlled perturbations) excite the downstream dynamics. With no forcing (only natural entrance noise), the behavior of the liquid film is reflected by the spatiotemporal diagram in Fig. 4. The average distance required for the film to undergo the primary instability is the healing length Δ. After this distance where the film is still uniform, a regular pattern appears with a constant wavelength (distance between two successive striations), velocity (constant slope of the striations), and frequency f_E. The frequency $f(x)$ is defined as the number of crests passing at the position x on the fiber in units of time and is measured with the linear camera oriented perpendicularly to the fiber. The evolution of the wave mean frequency with the distance x from the inlet is obtained by changing the position of the camera along the fiber and is shown in Fig. 5. The frequency is a constant f_E for about 5 cm; then the film undergoes secondary instabilities downstream and the wave evolution rapidly shows coalescence events which contribute to destabilization of the pattern and a decrease in the frequency. The regular pattern is consequently replaced by a disordered regime involving solitary waves sufficiently far downstream. The evolution of the thickness with time is given in Fig. 6 at three different locations. At the healing length [see Fig. 6(a)], primary waves are nearly sinusoidal. The power spectrum reveals a peak at the frequency f_E with a broadband noise level. Further downstream, these waves saturate and the spectrum peak broadens; rapidly, complex interactions or

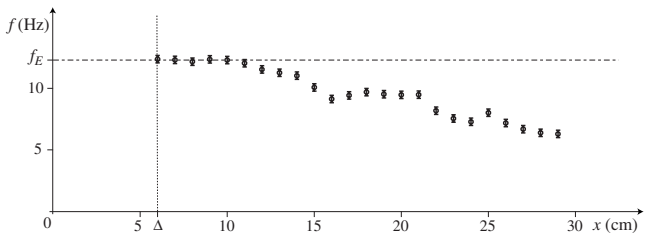

FIG. 5. Evolution of the frequency with the distance x on the fiber without forcing for $R=0.475$ mm and $h_N=0.78$ mm.

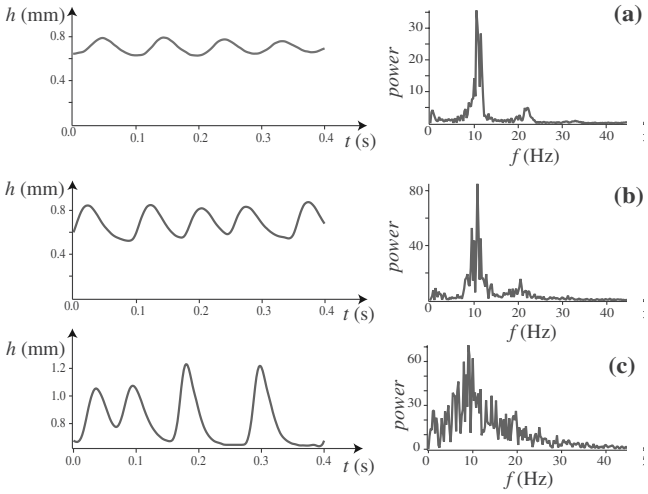

FIG. 6. Left: time series of the thickness for $R=1.5$ mm and $h_N=0.87$ mm ($R/l_c=1$ and $\tilde{\alpha}=0.58$) without forcing at (a) $x=8$ cm, (b) $x=30$ cm, and (c) $x=45$ cm. Right: corresponding spectra.

coalescence leads to a disordered flow [Figs. 6(b) and 6(c)]. Finally, fully developed waves tend to be isolated and present a steep front [Fig. 6(c)].

The typical shape of the axisymmetric structures tends also to vary with the flow rate and the curvature of the fiber depending on the dominant instability mechanism. For small fiber radii and low flow rates, the instability is governed by capillary effects and the Rayleigh–Plateau mechanism leads to the formations of beadlike structures sliding down a thin uniform liquid film [see Fig. 7(a)]. Though obviously affected by gravity, the front and back of the beads are rather symmetrical and we refer to them as *drops* and to the corresponding regime as the *droplike regime*. At large flow rates and fiber radii, the Kapitza instability dominates over the Rayleigh–Plateau instability mechanism. The front to back symmetry is clearly broken, the front being much sharper than the back of the structures [Fig. 7(b)]. The structures move on a much thicker substrate and have a shape that is reminiscent of the solitary waves observed on a film flowing down an inclined plane.[9] We may therefore refer to this regime as the *wavelike regime*. One aim of this study is to define criteria enabling to discriminate quantitatively between these two regimes.

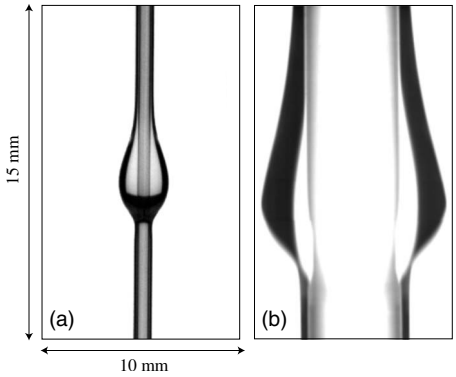

FIG. 7. (a) Droplike regime. (b) Wavelike regime.

C. Nusselt uniform film solution and dimensionless groups

Natural length scales for the problem are based on the geometry (radius R of the fiber) and the thickness h_N of the film at the inlet. Let us define a volumetric flow rate per circumference unit,

$$q_N = \frac{Q_m}{2\pi\rho R}. \tag{1}$$

Close to the inlet, the fiber is uniformly coated by the fluid which defines the characteristic flat-film thickness h_N as function of the flow rate q_N. Let us introduce a cylindrical coordinate system (r,θ,x) with r the radial coordinate, θ the azimuthal coordinate, and x the axial coordinate oriented with the flow in the downward direction. The velocity field is assumed to remain axisymmetric and its components in the axial and radial coordinates are denoted u_x and u_r. Balancing viscosity and gravity acceleration, the axial velocity u_x of a film of constant thickness is given by the Nusselt solution:

$$u_x = \frac{g}{\nu}\left[\frac{1}{2}(R+h_N)^2 \log\left(\frac{r}{R}\right) - \frac{1}{4}(r^2-R^2)\right]$$

$$\equiv \frac{g}{\nu}u_{x0}(r;R,h_N). \tag{2}$$

Integration of Eq. (2) across the film then gives

$$q_N = R^{-1}\int_R^{R+h_N} u_{x0} r dr = \frac{g}{\nu}\frac{h_N^3}{3}\phi(h_N/R), \tag{3}$$

where shape factor ϕ is a function of the aspect ratio $\tilde{\alpha}=h_N/R$ defined by

$$\phi(\tilde{\alpha}) = \frac{3[(1+\tilde{\alpha})^4(4\log(1+\tilde{\alpha})-3)+4(1+\tilde{\alpha})^2-1]}{16\tilde{\alpha}^3}. \tag{4}$$

The maximum speed is attained at the free surface $r=R+h_N$:

$$u_i = \frac{gh_N^2}{\nu}\left(\frac{2(1+\tilde{\alpha})^2\log(1+\tilde{\alpha})-\tilde{\alpha}(2+\tilde{\alpha})}{4\tilde{\alpha}}\right)$$

$$= \frac{gh_N^2}{6\nu}\left(\frac{3\phi(\tilde{\alpha})+\tilde{\alpha}\phi'(\tilde{\alpha})}{1+\tilde{\alpha}}\right). \tag{5}$$

Let us note that u_i is exactly equal to one-half of the *kinematic wave speed* c_k at which infinitesimal perturbations are transported by the flow in the small wavenumber limit.[8] Finally, we define the Nusselt velocity u_N as the ratio q_N/h_N. The vertical plane geometry corresponds to the limit of a very thin film $h_N \ll R$ so that $\phi(0)=1$. In this limit, the classical cubic dependence of the flow rate on the film thickness $q_N=(g/\nu)(h_N^3/3)$ and the classical relation $u_i/u_N=3/2$ are recovered.

The flow is then characterized by the Reynolds number $\mathrm{Re}=q_N/\nu$, the aspect ratio $\tilde{\alpha}=h_N/R$, and the Weber number $\mathrm{We}=\gamma/(\rho g h_N^2)=(l_c/h_N)^2$, where $l_c=\sqrt{\gamma/(\rho g)}$ is the capillary length. These dimensionless groups appear naturally when basic equations are made dimensionless using a length scale corresponding to h_N. However, an alternative scaling has been proposed by Shkadov[10] for film flows down an incline and later on adapted to the cylindrical geometry.[8,11] Shkadov's idea was to compress the streamwise coordinate by balancing gravity, viscous drag, and pressure gradient induced by surface tension, which gave a compression factor $\kappa=\mathrm{We}^{1/3}$ corresponding to the ratio of the streamwise length scale κh_N to the Nusselt film thickness h_N. Whenever streamwise viscous diffusion is negligible, the set of dimensionless groups is then reduced from 3 to only 2: $\tilde{\alpha}$ and the reduced Reynolds number $\delta=3\,\mathrm{Re}/\kappa$ that is a composite parameter combining inertia, viscosity, and surface tension.

Finally, the linear stability analysis of the Nusselt flat-film solution in the inertialess limit ($\mathrm{Re}\ll 1$) brings out another composite parameter that compares the characteristic time of growth τ_g of linear perturbations to the advection time τ_a of a structure over its length:[7,8]

$$\beta^\star = (\tau_a/\tau_g)^{2/3} = \left[\frac{3u_N}{2u_i}\frac{\tilde{\alpha}}{(1+\tilde{\alpha})^4}\right]^{2/3}(l_c/R)^{4/3}. \tag{6}$$

This parameter is a generalization of the parameter $\beta=\tilde{\alpha}^{2/3}(l_c/R)^{4/3}$ introduced by Kalliadasis and Chang[12] in their study of the drop formation process corresponding to the experiments by Quéré.[3] Quéré observed that the Rayleigh–Plateau instability of a thin film flowing down a fiber can be arrested by the mean flow of the film when the film thickness h_N is sufficiently thin in comparison to the ratio R^3/l_c^2. Assuming small film thicknesses with respect to the fiber radius ($\tilde{\alpha}\ll 1$), Kalliadasis and Chang showed that Quéré's observations are in remarkable agreement with the condition $\beta<\beta_c\approx 1.413$ obtained from a matched asymptotic analysis of the nonlinear solutions. Notice that in this limit, $\beta^\star$ simplifies to β:

$$\lim_{\tilde{\alpha}\to 0}\beta^\star/\beta = 1. \tag{7}$$

The arrest of the growth of the Rayleigh–Plateau instability by the flow advection was referred to as a *saturation* mechanism by Quéré. For this reason, we may refer to $\beta^\star$ and β as saturation numbers.

D. Flow regime diagram

A tentative diagram of the expected flow regimes is presented in Fig. 8. The diagram is drawn in the plane R/l_c versus $\tilde{\alpha}=h_N/R$ for practical use. The aspect ratio $\tilde{\alpha}$ can be varied by changing the flow rate independently to the ratio R/l_c, which in turn can easily be varied by replacing the fiber. Another advantage of this choice lies in the definition of the saturation number $\beta^\star$ which is a function of $\tilde{\alpha}$ and R/l_c only. The curve of equation $\beta^\star=1$ is labeled "c" in Fig. 8 and separates the plane $(R/l_c,\tilde{\alpha})$ into two regions. At the left hand side of the curve c, $\beta^\star$ is larger than 1 and the characteristic time of growth of the Rayleigh–Plateau instability τ_g is smaller than the characteristic time needed to displace the waves over their length, τ_a. [The variation of $\beta^\star$ in the plane $(R/l_c,\tilde{\alpha})$ is figured by an arrow.] One then expects that the Rayleigh–Plateau instability mechanism dominates over the flow advection in that region in dark and light

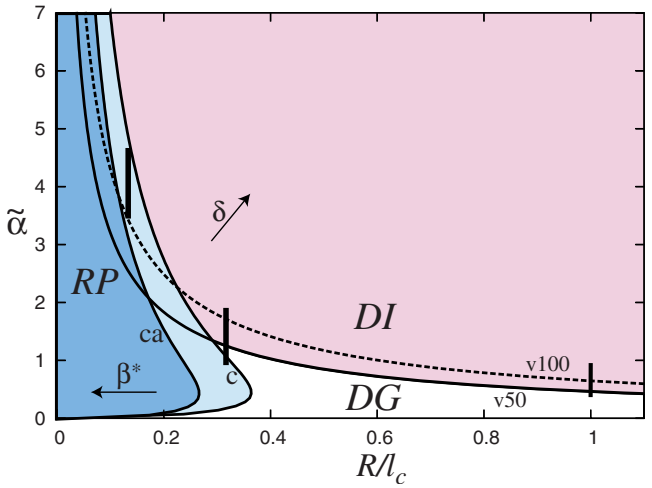

FIG. 8. (Color online) Flow regime diagram in the parameter space R/l_c and $\tilde{\alpha}$. The curves are the loci of $\delta=1$, $\beta^\star=1$, and $\beta^\star=\beta^\star_{ca}\approx 1.507$. RP refers to the Rayleigh–Plateau droplike regime, DG to the drag-gravity regime, and DI to the drag-inertia regime. The wavelike regime takes place in the union of the DI and DG regions. Vertical segments represent the experiments discussed in this study.

gray and labeled "RP" in Fig. 8. Our experiments show that indeed, the droplike structures shown in Fig. 7(a) are observed for parameters $\tilde{\alpha}$ and R/l_c lying in the RP region. Conversely, at the right of the curve c, the advection by the flow may saturate the Rayleigh–Plateau instability. The wavelike structure presented in Fig. 7(b) corresponds to $\beta^\star<1$.

As already noticed, the reduced Reynolds number δ compares inertia effect to viscosity and surface tension. This parameter can be expressed as a function of the aspect ratios $\tilde{\alpha}$ and R/l_c and the Kapitza number $\Gamma=\sigma/(\rho\nu^{4/3}g^{1/3})$:

$$\delta = 3\ \mathrm{Re}/\kappa = \Gamma^{3/2}(\tilde{\alpha}R/l_c)^{11/3}\phi(\tilde{\alpha}). \tag{8}$$

Note that the Kapitza number $\Gamma=(l_c/l_\nu)^2$ can also be expressed in terms of the ratio of two lengths: the capillary length l_c and the viscous-gravity length $l_\nu=(\nu^2/g)^{1/3}$ so that δ is a function of the three length ratios $\tilde{\alpha}$, R/l_c, and l_c/l_ν. By looking at the tail length of solitary waves, Takeshi[13] showed that in the planar geometry $\delta\approx 1$ signals the transition between the *drag-gravity regime*, for which inertia and surface tension play a perturbative role compared to viscous drag and gravity, to the *drag-inertia regime*, where inertia becomes dominant. The curves $\delta=1$ corresponding to the silicon oil v50 ($\Gamma=5.48$) is labeled "v50" and divides the region of the plane $(\tilde{\alpha},R/l_c)$ corresponding to the wavelike regime into two (see Fig. 8). In the medium gray region labeled "DI," inertia is expected to be dominant ($\delta>1$ and $\beta^\star<1$). Following Ref. 14 where an asymptotic analysis of solitary waves flowing down a vertical plane is offered for $\delta\gg 1$, the drag-inertia regime should be characterized by large-amplitude solitary waves with a wave speed that is proportional to the average speed of the film of uniform thickness, or *substrate*, on which the wave travels. Below the curve $\delta=1$ and at the right of the curve $\beta^\star=1$ lies a region colored in white and labeled "DG" in Fig. 8. Region DG corresponds to the drag-gravity regime where the balance of viscous drag and gravity is only weakly affected by the Kapitza and Rayleigh–Plateau instability mechanisms ($\delta<1$ and $\beta^\star<1$). In that region of the plane of parameters, we expect to see wavelike structures of relatively small amplitude.

The flow regime diagram presented in Fig. 8 is completed by the curve $\beta^\star=\beta^\star_{ca}\approx 1.507$ labeled "ca" which identifies the convective to absolute transition in the inertialess limit.[7] Comparisons to the Orr–Sommerfeld analysis of the linearized basic equations around the Nusselt solution show good agreement with the threshold $\beta^\star=\beta^\star_{ca}$ for viscous fluids such as the Rhodorsil silicon oil v50 employed in our experiments. The regions of the plane $\tilde{\alpha}$ versus R/l_c located at the left hand side of the curve $\beta^\star=\beta^\star_{ca}$ (dark gray region) thus corresponds to the onset of a self-sustained dynamics of the flow prompted by an absolute instability of the Nusselt uniform film. Conversely, for $\beta^\star<\beta^\star_{ca}$ the convective instability of the film gives way to a noise-driven dynamics illustrated in Figs. 4–6.

Notice that a film flowing down a vertical plane, which undergoes the Kapitza instability, is only convectively unstable.[15] The absolute nature of the instability is thus related to the Rayleigh–Plateau instability prompted by the cylindrical geometry. We have therefore single out the region of the plane located in between the curves c, $\beta^\star=1$, and ca, $\beta^\star=\beta^\star_{ca}$, for which the dynamics of the primary instability is convective but the dominant instability mechanism is the Rayleigh–Plateau mechanism.

Let us stress that the curves c and ca corresponding to levels of the function $\beta^\star(R/l_c,\tilde{\alpha})$ are independent of the fluid properties whereas the locus $\delta=1$ moves with the Kapitza number. The curve labeled "v100" in Fig. 8 and corresponding to silicon oil v100 ($\Gamma=2.2$) illustrates the displacement of the locus $\delta=1$ with the Kapitza number. The delimitation of the different regimes using the curves $\delta=1$ and $\beta^\star=1$ is only indicative. We do not expect the transitions from drag-gravity to drag-inertia regimes and from droplike to wavelike regimes to occur exactly along these curves. Transitions should be observed at $\delta=O(1)$ and $\beta^\star=O(1)$ for values that are still to be determined and not exactly for parameter values equal to 1.

The purpose of this study is to examine the response of the film to an inlet excitation. We will limit ourselves to convectively unstable situations for which the primary instability responds to the inlet signal. By controlling the inlet forcing, our goal is to generate and characterize trains of traveling waves that propagate at constant speed and shape on a sufficiently long part of the fiber. The dynamics of the global mode triggered by the absolute instability of the film is thus left for future study. The three different fibers considered in this work have been chosen in order to explore different regions of the flow regime diagram at the right hand side of the curve $\beta^\star=\beta^\star_{ca}$ and correspond to the ratios $R/l_c=0.12$, 0.32, and 1. In practice, the interval of reachable flow rates, and thus of reachable aspect ratios $\tilde{\alpha}$—figured in Fig. 8 by vertical segments—is limited by the design of the entrance valve and by the onset of the absolute

instability (curve ca). In particular, silicon-oil films flowing down the fiber of radius $R=0.2$ mm ($R/l_c=0.12$) should be driven by the Rayleigh–Plateau instability, whereas we expect a dynamics driven by the Kapitza instability for the thick fiber of radius equal to 1.5 mm ($R/l_c=1$). The fiber of intermediate radius $R=0.475$ mm ($R/l_c=0.32$) has been chosen to examine the combined effect of the two instability mechanisms.

III. WEIGHTED RESIDUAL MODELING

In a previous paper,[8] a reduced set of two evolution equations for the film thickness h and the flow rate q has been proposed to model the spatiotemporal evolution of the film. In this section, we briefly recall the main steps leading to the formulation of this model and the main results obtained in Ref. 8.

Various models have been proposed within the framework of the lubrication theory by making use of the large aspect ratio between the typical length of the wave λ and the film thickness h, hence the introduction of a film parameter $\epsilon \ll 1$ measuring slow variations in time and space and the expansion of the flow variables with respect to ϵ. Frenkel[16] thus derived an evolution equation for the film thickness in the case where the film is very thin compared to the radius of the fiber and inertia is neglected. Some authors[5,6] relaxed the assumption of thin film but neglected inertia. Inertial effects were initially considered by Trifonov[17] using the Kármán–Polhausen averaging procedure. The result is an extension to the axisymmetric geometry of the integral boundary-layer (IBL) equations or Shkadov equations that model the dynamics of a falling film on inclined planes.[9,18]

For all these models, the contributions of the streamwise viscous diffusion are neglected. Yet, the dispersive effect of the streamwise viscous diffusion has already been evidenced.[8] For this reason, streamwise viscous diffusion is also referred to as *viscous dispersion*. Besides, IBL equations are well known to incorrectly predict the instability onset of a falling film on an inclined plane. This discrepancy arises from the neglect of the deviations of the velocity profile from its parabolic shape induced by the deformations of the free surface as shown in Ref. 19. Following Shkadov's initial idea of expanding the velocity field on a set of polynomials and applying a weighted residual procedure, the shortcomings of the Shkadov equations can be cured. The obtained models can be classified as weighted residual integral boundary-layer (WRIBL) equations.[20]

In Ref. 8, the WRIBL approach is extended to the axisymmetric geometry. Equations are made dimensionless using the Nusselt film thickness h_N in the radial direction r and κh_N in the streamwise direction x, with a scale ratio $\kappa=\mathrm{We}^{1/3}=(l_c/h_N)^{2/3}$. The time scale is defined as $3q_N/h_N=gh_N^2\phi(\tilde{\alpha})/\nu$. This choice of scales introduces the reduced Reynolds number δ, the saturation number β, and a viscous dispersion parameter $\eta\equiv 1/\kappa^2=(h_N/l_c)^{4/3}$ The obtained averaged axial momentum equation reads

$$\begin{aligned}\delta\partial_t q = {} & \delta\left[-F(\tilde{\alpha}h)\frac{q}{h}\partial_x q + G(\tilde{\alpha}h)\frac{q^2}{h^2}\partial_x h\right] \\ & + \frac{I(\tilde{\alpha}h)}{\phi(\tilde{\alpha})}\left[-\frac{3\phi(\tilde{\alpha})}{\phi(\tilde{\alpha}h)}\frac{q}{h^2} + h\left\{1+\partial_{xxx}h\right.\right. \\ & \left.\left. + \frac{\beta}{(1+\tilde{\alpha}h)^2}\partial_x h - \frac{1}{2}\partial_x\left(\frac{\tilde{\alpha}}{1+\tilde{\alpha}h}(\partial_x h)^2\right)\right\}\right] \\ & + \eta\left[J(\tilde{\alpha}h)\frac{q}{h^2}(\partial_x h)^2 - K(\tilde{\alpha}h)\frac{\partial_x q\partial_x h}{h} - L(\tilde{\alpha}h)\frac{q}{h}\partial_{xx}h\right. \\ & \left. + M(\tilde{\alpha}h)\partial_{xx}q\right], \end{aligned} \tag{9}$$

where the shape factor ϕ is defined in Eq. (4). Coefficients F, G, I, J, K, L, and M are functions of the aspect ratio $\tilde{\alpha}=h_N/R$ defined in the Appendix.

Equation (9) is completed by the (exact) mass balance of a plane section of fluid,

$$\partial_t h = -\frac{1}{1+\tilde{\alpha}h}\partial_x q. \tag{10}$$

Apart from the neglected second-order inertial corrections induced by the deviations of the velocity field from the Nusselt distribution (2), the averaged momentum equation (9) is consistent up to order ϵ^2. The model (10) and (9) accounts for inertia, wall friction, gravity, surface tension, and viscous dispersion effects [last row in Eq. (9)]. Besides, it is consistent with the inertialess evolution equation derived by Craster and Matar.[6] This equation referred hereafter as the CM equation is recovered by setting δ and η to zero in Eq. (9), from which an explicit expression of q as a function of h and its derivatives is obtained. Substitution of this expression into the mass balance (10) finally gives the CM equation:

$$\partial_t\left(h+\frac{\tilde{\alpha}}{2}h^2\right) + \partial_x\left[\frac{h^3}{3}\frac{\phi(\tilde{\alpha}h)}{\phi(\tilde{\alpha})}\left(1+\frac{\beta}{(1+\tilde{\alpha}h)^2}\partial_x h + \partial_{xxx}h\right)\right] = 0. \tag{11}$$

We expect to obtain a fair agreement with experimental data using the simple CM equation (11) when the Rayleigh–Plateau instability dominates over the inertia and viscous dispersion effects, whereas we need to turn to the more refined WRIBL model in order to capture those effects.

IV. PRIMARY INSTABILITY

A first check of the accuracy of the WRIBL model (10) and (9) consists of the spatial stability analysis of the primary instability of the Nusselt uniform film flow. We perform a normal mode analysis $h=1+\epsilon\tilde{h}\exp[i(kx-\omega t)]$ and $q=1/3+\epsilon\tilde{q}\exp[i(kx-\omega t)]$, where $k=k_r+ik_i$ is complex, ω is real, and $\epsilon\ll 1$, leading to a dispersion relation of the form $D(k,\omega)=0$ provided in Ref. 8. In Fig. 9 we present the spatial growth rate $-k_i$ as a function of the frequency $f=\omega/(2\pi)$ for spatially amplified harmonic perturbations obtained from the linear stability analysis of the WRIBL model (10) and (9). Comparisons to the linear stability analysis based on the primitive equations, i.e., to the solutions to the

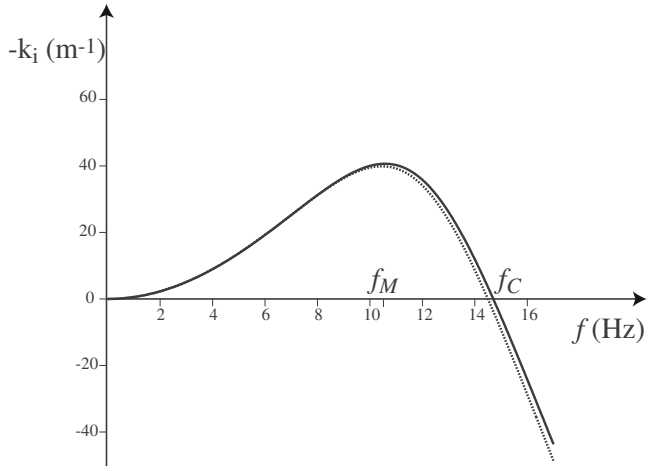

FIG. 9. Spatial growth rate vs frequency for $R=1.5$ mm and $h_N=0.87$ mm ($R/l_c=1$ and $\tilde{\alpha}=0.58$). Plain line: solution to the OS equations. Dashed line: linear stability analysis of the WIRBL model (10) and (9).

Orr–Sommerfeld (OS) problem, show good agreement (the OS analysis of the film in the cylindrical geometry is given in Ref. 21). Due to the damping of high frequencies by surface tension, only the range of frequencies ranging from 0 to the cut-off frequency f_c are amplified ($-k_i>0$) which signals the long-wave nature of the instability. Note that the results obtained with the WRIBL model are in remarkable agreement with those from the linear stability of the primitive equations. Both present a maximum at a frequency f_M referred to as the frequency of maximum response.

In Fig. 10, the cut-off frequency f_c and frequency of maximum response f_M are compared to the experimental data. The mean frequency f_E of the primary wavetrain, defined by counting the number of crests per unit of time at $x=\Delta$, compares well with the frequency of maximum response f_M. We identify the experimental cut-off frequency, denoted by f_{CE}, as the frequency at which the forcing stops affecting the inception region of the flow. When the flow is excited at the inlet at a forcing frequency f_{for} below the cut-off frequency ($f_{\text{for}}<f_{CE}$), the inception region of the flow synchronizes at the forcing frequency and an initially regular wavetrain is generated with a constant healing length Δ depending on the level of the forcing amplitude. Above the

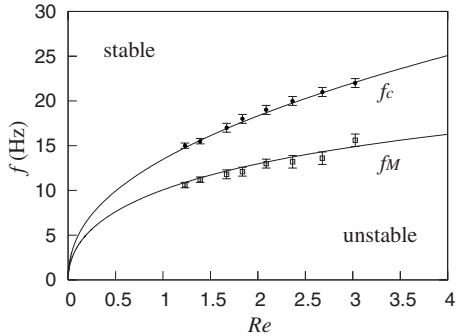

FIG. 10. Maximum frequency f_M and cut-off frequency f_C vs Reynolds number Re for $R=0.475$ mm ($R/l_c=0.32$). The plain line refers to solutions of the OS equation and the dotted line refers to the experimental data.

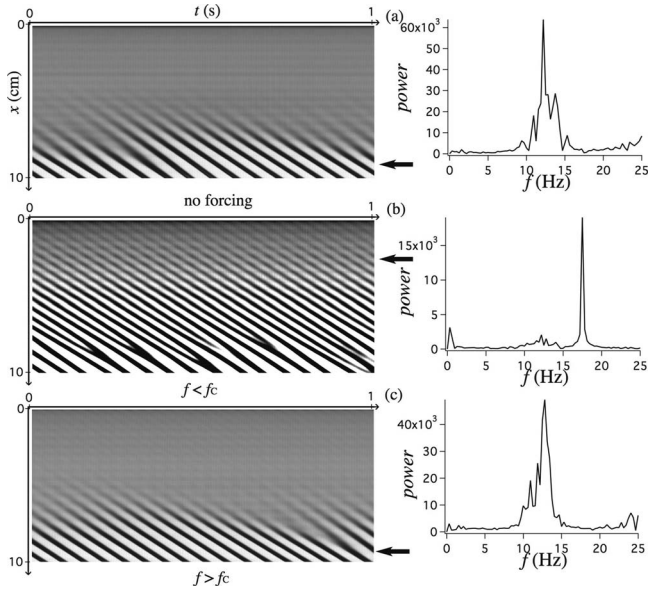

FIG. 11. Experiments showing the response of the inception region of the flow (a) without forcing and with forcing at (b) $f_{\text{for}}=17.5$ Hz$<f_{CE}$ and (c) $f_{\text{for}}=18.5$ Hz$>f_{CE}$. Left: Spatiotemporal diagrams. Right: power spectra. The locations at which the time series have been recorded are indicated by arrows. $R=0.475$ mm and $h_N=0.78$ mm ($R/l_c=0.32$ and $\tilde{\alpha}=1.64$).

cut-off frequency, for $f_{\text{for}}>f_{CE}$, the flow behaves as if there was no forcing: the healing length fluctuates in time and the frequency of the primary wavetrain is equal to f_M with a larger spectrum characteristic of a natural response (see Fig. 11). Figure 10 compares satisfactorily f_{CE} to the cut-off frequency f_c computed from the linear stability analysis.

V. NONLINEAR RESPONSE TO PERIODIC FORCING

As discussed in Sec. IV, the inception region of the flow can be synchronized by applying a periodic inlet forcing. We further discuss here the nonlinear evolution of the emerging primary wavetrain as it propagates downstream.

A. Spatial evolution of periodic waves

Depending on the forcing frequency f_{for}, three types of response of the film dynamics have been identified. These three different responses are illustrated in Fig. 12 for the fiber of radius $R=1.5$ mm (similar observations have been made for $R=0.2$ mm and $R=0.475$ mm).

At a forcing frequency close to the frequency f_M of maximum response predicted by the linear stability analysis, the system responds precisely to the forcing frequency and the wave pattern is regular on the whole length of the fiber that is about 1 m long [see Fig. 12(a)]. Time series recorded at three locations on the fiber ($x=8$, 18, and 30 cm) reveal a wave shape that is not significantly affected by the saturation nonlinear mechanism. A comparison between the two power spectra at $x=8$ cm and $x=18$ cm reveals, however, a slight redistribution of the energy of the signal between the forcing frequency and its overtones in favor of the forcing frequency. This redistribution corresponds to the largest growth rate associated with $f_{\text{for}}\sim f_M$. Further downstream ($x=30$ cm), the

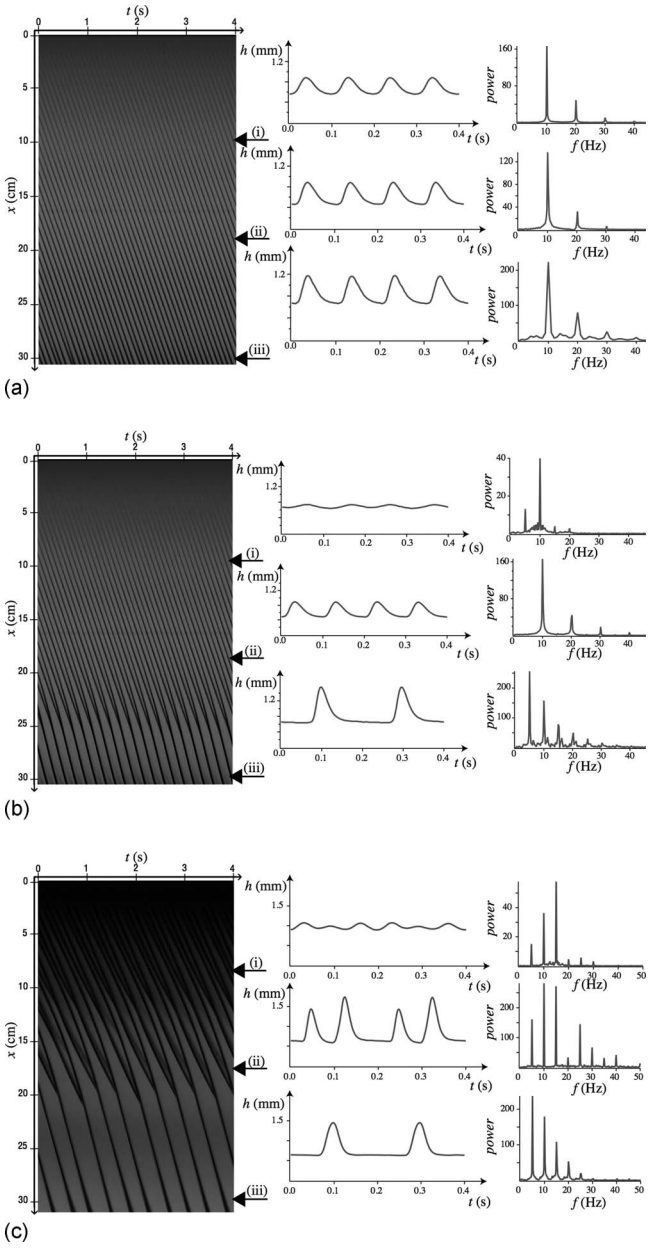

FIG. 12. Experimental responses to inlet forcing ($R=1.5$ mm and $R/l_c=1$). Left: spatiotemporal diagrams. Right: time series and power spectra of the thickness at three locations on the fiber (indicated by arrows in the left panels): (i) $x=8$ cm, (ii) $x=18$ cm, and (iii) $x=30$ cm.

nonlinear saturation process favors the growth of overtones. The observed synchronized dynamics of the film at the forcing frequency is made possible by the small amount of noise introduced at the inlet (recall that the thickness fluctuations due to ambient noise are limited to $10^{-3}\%$). Yet, the broadening of the spectrum peaks which is observable on the power spectra is due to the amplification of the ambient noise by the flow.

The second type of response occurs for forcing frequencies smaller than f_M. In that case, the system needs two or three steps to finally respond to the forcing frequency. A two-step scenario for a forcing frequency $f_{\text{for}}=5$ Hz $\simeq f_M/2$ is depicted in Fig. 12(b). The system responds first at the first overtone $2f_{\text{for}}\simeq f_M$ as a quasi-sine-wave (see the power spectrum at $x=8$ cm). Further downstream, at $x=18$ cm, waves have grown and depart from the sine shape. Overtones have grown whereas the first harmonic at f_{for} has been damped. The second step leading to the formation of a regular wavetrain at f_{for} consists of a sequence of coalescence events that occur periodically at a fixed location ($\approx$25 cm). Coalescence events are accompanied by an acceleration of the waves and an increase in the wavelength. A localization of the structures separated by nearly flat substrates is observable in the time series at $x=30$ cm.

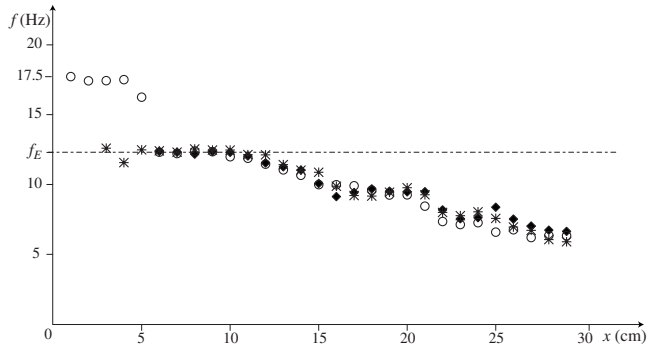

FIG. 13. Frequency f vs distance x for $R=0.475$ mm and $h_N=0.78$ mm ($R/l_c=0.32$ and $\tilde{\alpha}=1.64$) without forcing (black polygons), $f_{\text{for}}=17.5$ Hz (circles), and $f_{\text{for}}=18.5$ Hz (crosses)

An example of a three-step response to inlet forcing is shown in Fig. 12(c). The primary wavetrain emerging from the inception region is regular with a frequency $f=3f_{\text{for}}$. The power spectrum of the time series at $x=8$ cm is characteristic of a sine wave at $f=3f_{\text{for}}$ modulated by two envelopes of frequencies f_{for} and $2f_{\text{for}}$. A first series of periodic coalescence events is visible at a fixed location $x\approx 11$ cm leading to the reduction by one-third of the number of visible crests. The wave shape at $x=18$ cm is highly nonlinear as reflected by the large number of overtones found in the corresponding power spectrum. A second periodic sequence of coalescence events is observable further downstream at $x\approx 19$ cm. The resulting wavetrain is synchronized at the forcing frequency $f=f_{\text{for}}$ and travels much faster than the primary wavetrain. Notice the nearly flat substrate in between the pulses. When compared to the experiments presented in Figs. 12(a) and 12(b), the three-step nonlinear response of the film shown in Fig. 12(c) has been obtained at a larger flow rate for which the frequency of maximum response is also larger ($f_M=15.6$ Hz). We had indeed difficulties in sufficiently exciting the film at low frequency for two reasons: (i) the low-frequency pressure perturbations produced by our vibrating device in the supply tank is partly smoothed by the entrance valve and (ii) amplification by the primary instability of inlet perturbation is insufficient to synchronize the flow. For the two above reasons, it has not been possible to obtain a time-periodic spatial response with inlet forcing at low frequency.

Finally, the last type of response concerns forcing frequencies close to the cut-off frequency f_{CE}. When f_{for} is above the cut-off frequency, we have already noted that the inception region of the flow ceases to respond to a forcing applied at the inlet. This is also true below the inception region for $f_{\text{for}}\lessapprox f_{CE}$. In Fig. 13, we show the evolution with

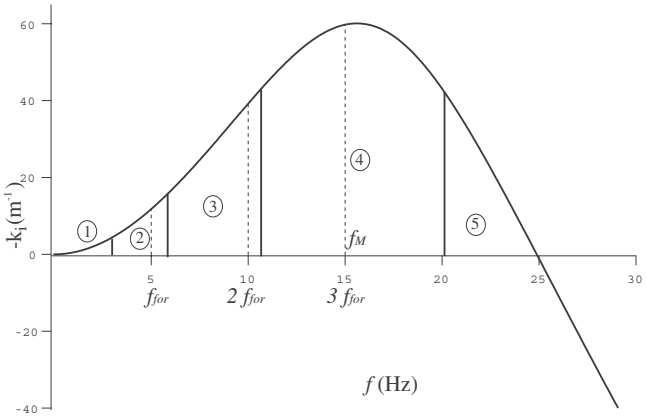

FIG. 14. Sketch of the different nonlinear responses to a periodic forcing at frequency f_{for}. The spatial growth rate vs frequency is plotted for $R=1.5$ mm and $h_N=1.14$ mm ($R/l_c=1$ and $\tilde{\alpha}=0.76$). Dashed lines refer to the frequency of the fundamental $f_{for}=5$ Hz and to the overtones corresponding to the experiment discussed in Fig. 12(c).

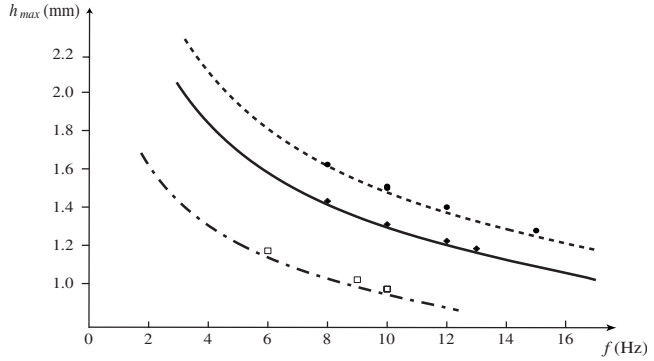

FIG. 15. Maximum amplitude h_{max} of traveling waves vs forcing frequency f_{for} for $R=0.475$ mm and three different Nusselt thicknesses: $h_N=0.68$ mm (dashed dotted line), $h_N=0.83$ mm (plain line), and $h_N=0.88$ mm (dashed line). The curves correspond to the solutions to the WRIBL model (10) and (9) and the points to the experimental data.

the position of the mean number of crests passing at a location x [the frequency $f(x)$] along the fiber in the vicinity of the cut-off frequency ($f_{CE}\approx 18$ Hz for $R=0.475$ mm and $h_N=0.78$ mm). At $f_{for}=17.5$ Hz, the flow starts to respond to the forcing on the first 5 cm, then rapidly recovers its natural behavior. The statistics of the crests passing at a given station is unaffected by the forcing as suggested by the superposition of the mean distribution of crests $f(x)$ with and without forcing.

Figure 14, deduced from the linear stability analysis, summarizes the different observed responses of the film to a periodic forcing at inlet. The transition from one type of response to another depends on the relative growth rate of the forcing signal at frequency f_{for} in the inception region compared to the maximum of the growth rate at frequency f_M. More precisely, the observed dynamics results from the competition between the amplification of the inlet noise, the fundamental frequency of the forcing signal, and its overtones. We illustrate this competition with the distribution of the growth rate with respect to the frequency for the parameters corresponding to the experiment shown in Fig. 12(c). Plain vertical lines delimit five zones in our diagram. In the first zone, at low forcing frequency, the amplification of the imposed signal at the inlet is too weak to overcome the growth of the frequency content of the noise around f_M, which is strongly amplified by the primary instability. In the second (third) region of the diagram, the second (first) overtone corresponds to a frequency close to the maximum of amplification, i.e., $3f_{for}\approx f_M$ ($2f_{for}\approx f_M$) which explains that the frequency of the primary wavetrain is $3f_{for}$ ($2f_{for}$). The subsequent nonlinear transfer of energy from the overtones to the fundamental is responsible for the periodic sequences of coalescence events leading to the final synchronization of the wavetrain at the fundamental frequency observed in Figs. 12(b) and 12(c). In the fourth region, f_{for} is close to f_M and the inlet forcing signal is then as strongly amplified by the primary instability as the ambient noise which explains that a synchronization of the flow can be observed over the whole fiber. Finally, in the fifth region of the diagram corresponding to $f_{for}\approx f_c$, only the fundamental frequency of the forcing signal is amplified by the primary instability. As f_{for} approaches the cut-off frequency f_{CE} the spatial growth rate decreases rapidly to zero which explains that the ambient noise—being strongly amplified—destabilizes the primary wavetrain soon after the inception region.

To conclude this section, let us discuss the influence of the amplitude of the forcing signal on the dynamics of the flow. When the primary instability responds to the forcing (regions 2–5 in Fig. 14), the healing length Δ tends to decrease as the forcing amplitude increases. Another effect of an increase in the fluttering amplitude of the vibrating device is an extension of the frequency content of the signal, more overtones being produced. As a result, the periodic sequence of coalescence events tends to occur closer to the inlet and the synchronization of the flow at the fundamental frequency f_{for} is also observed earlier.

B. Characteristics of the traveling waves

Our experiments show that in a certain range of frequencies around the frequency of maximum response f_M, a periodic forcing at the inlet is able to synchronize the flow to the forcing frequency. The resulting wavetrain consists of periodic traveling waves. In this section we consider the characteristics (speed, amplitude, and shape) of experimental traveling waves and compare them to the solutions of the two-equation WRIBL model (10) and (9).

1. On the shape

The evolution of the maximum thickness h_{max} with the forcing frequency is shown in Fig. 15 for three different flow rates. The maximum thickness decreases with the frequency. h_{max} follows the same trend as the Nusselt thickness and increases with the flow rate. Traveling wave solutions to the WRIBL model are limit-cycle trajectories of the corresponding three-dimensional dynamical system (details are given in a companion paper). They have been numerically obtained by continuation using software AUTO07P and its extension HOMCONT.[22,8] Continuations have been initialized with infinitesimal neutral waves obtained from the linear stability

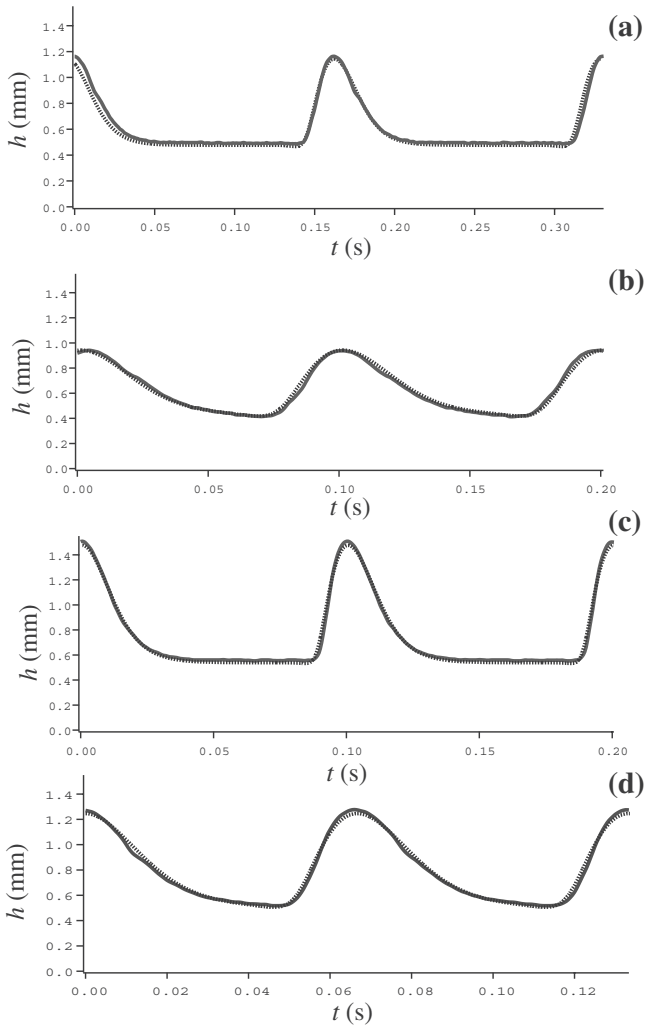

FIG. 16. Wave profiles of traveling waves for $R=0.475$ mm ($R/l_c=0.32$). Solid and dashed lines refer to the experimental time series and to solutions to the WRIBL model, respectively. From top to bottom: $h_N=0.68$ mm ($\tilde{\alpha}=1.43$) and $f_{\text{for}}=6$ Hz; $h_N=0.68$ mm and $f_{\text{for}}=10$ Hz; $h_N=0.88$ mm, ($\tilde{\alpha}=1.85$) and $f_{\text{for}}=10$ Hz; $h_N=0.88$ mm and $f_{\text{for}}=15$ Hz.

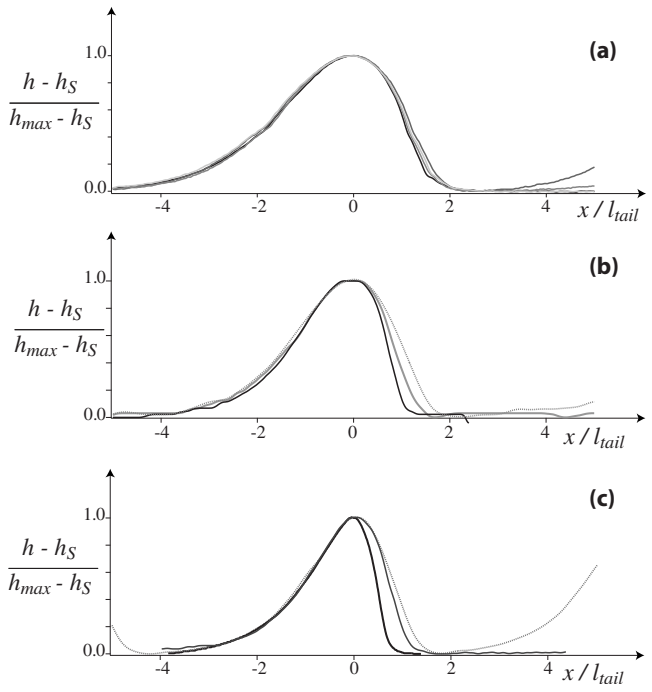

FIG. 17. Normalized profiles with respect to the amplitude $h_{\max}-h_s$ and tail length l_{tail}. Upper panel: $R=0.2$ mm and $h_N=0.84$ mm and from light to dark curves $f_{\text{for}}=6$, 8, and 9 Hz and natural evolution (see also the caption of Fig. 18). Middle panel: $R=0.475$ mm and $f_{\text{for}}=7$ Hz and from light to dark curves $h_N=0.62$, 0.76, and $h_N=0.86$ mm. Lower panel: $R=1.5$ mm and from light to dark curves $h_N=0.87$ mm, $f_{\text{for}}=4$, and 10 Hz and natural evolution for $h_N=0.93$ mm.

analysis. A constant averaged flow rate $\langle q\rangle=T^{-1}\int_0^T qdt$ (T refers to the period) has been enforced to fit experimental open-flow conditions.[8] Comparisons to experimental data of the maximum thickness of the numerical solutions show an excellent agreement.

Two experiments for two different flow rates and two forcing frequencies illustrate the influence of the inlet frequency and flow rate on the shape of the traveling waves. The four time series presented in Fig. 16 have been recorded with a resolution in thickness of ± 0.02 mm and a temporal resolution of $\approx 10^{-3}$ s. At a given flow rate, lowering the frequency sharpens the wave front and enhances the wave amplitude. Low-frequency waves become solitarylike with a profile made of isolated humps separated by a substrate of uniform thickness. Conversely, at a given frequency, increasing the flow rate has a similar effect on the wave shape and amplitude, the waves evolving to more localized structures. Experimental wave profiles have been compared to the solutions to the WRIBL model at the same frequency and averaged flow rate (dotted curves in Fig. 16) showing again a convincing agreement.

In Ref. 8, we have already stressed the damping effects of viscous dispersion on the capillary waves preceding the beads. This explains that, in contrast with former studies devoted to falling films on planar substrates,[23–25] capillary ripples have not been observed ahead of the waves. Indeed, experimental investigations of films flowing down an inclined plane were conducted with low viscosity and high surface tension working fluids (glycerin and water mixture or alcohol). The capillary length is generally large and the film thickness is small so that the viscous dispersion parameter $\eta=(h_N/l_c)^{4/3}$ is small. Yet, we cannot exclude the possibility of a too low resolution preventing us from detecting small capillary waves. Solitarylike waves displayed in Fig. 16 ($h_N=0.68$ mm, $f_{\text{for}}=6$ Hz and $h_N=0.88$ mm, $f_{\text{for}}=10$ Hz) do present at least one tiny ripple ahead of the bead.

To characterize the wave shape, we define the length of the upstream tail l_{tail} with an exponential fit $e^{x/l_{\text{tail}}}$. Wave profiles obtained at different experimental conditions can easily be compared one to another with reference to the wave amplitude $h_{\max}-h_s$ and the tail length l_{tail}. The normalized profiles $(h-h_s)/(h_{\max}-h_s)$ as a function of the reduced distance x/l_{tail} have been reported in Fig. 17. Figure 17(a) compares wave profiles obtained with a fiber of radius $R=0.2$ mm and silicon oil v100. Corresponding time series of the film thickness are shown in Fig. 18. Panel (a) is a record at the bottom end of the fiber of the solitary waves observed as the final

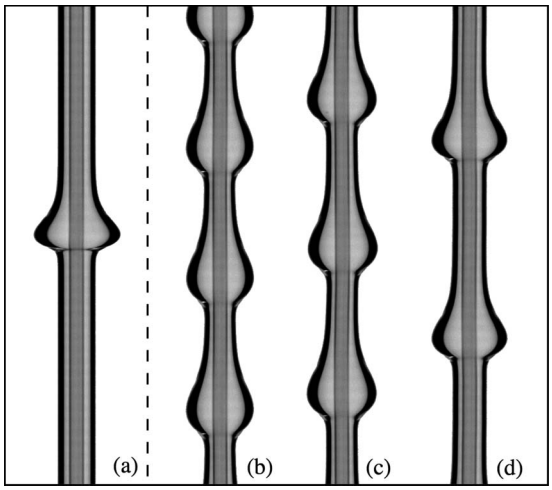

FIG. 18. Time series from the linear camera recorded at a distance $x=75$ cm from the inlet. $R=0.2$ mm and $h_N=0.84$ mm ($R/l_c=0.12$ and $\tilde{\alpha}=4.2$); (a) natural evolution (no forcing), (b) $f_{\text{for}}=9$ Hz, (c) $f_{\text{for}}=8$ Hz, and (d) $f_{\text{for}}=6$ Hz.

result of the natural evolution of the film flow when no forcing has been applied. Panels (b)–(d) are traveling waves excited by a forcing at the inlet. A variation of the thickness of the substrate h_s ($0.41\ \text{mm} \leq h_s \leq 0.54\ \text{mm}$) and of the maximum thickness ($1.21\ \text{mm} \leq h_{\max} \leq 1.54\ \text{mm}$) has been observed. Yet, the normalized profiles of the beads are nearly identical. The saturation number and reduced Reynolds number based on the substrate thickness vary within the ranges $0.1 < \delta_s < 0.35$ and $1.7 < \beta_s^\star < 2.2$ which suggests that the Rayleigh–Plateau instability mechanism dominates over the Kapitza instability mode. We therefore conclude that beads driven by the Rayleigh–Plateau instability seem to have a generic shape.

Figure 17(b) compares the normalized shape of waves observed on the fiber of intermediate radius $R=0.475$ mm when a low-frequency forcing ($f_{\text{for}}=7$ Hz) is applied. This time, clear differences can be noticed, a steepening of the wave front being observed as the Nusselt thickness (and the substrate thickness) increases. A similar steepening is observed with the localization of the beads when the frequency is varied (not shown). Parameters based on the substrate thickness suggest that the two instability mechanisms are important ($0.94 \leq \beta_s^\star \leq 1.1$ and $0.22 \leq \delta_s \leq 0.85$). Turning to the largest tested fiber ($R=1.5$ mm), we have compared in Fig. 17(c) the wave profiles obtained at a low frequency ($f_{\text{for}}=4$ Hz) and at a relatively high one ($f_{\text{for}}=10$ Hz) to the solitary waves observed at the downstream end of the fiber and resulting from the natural evolution of the flow. A steepening of the wave front with the localization of the beads is again observed. Parameter values ($\beta_s^\star \approx 0.25$ and $0.82 \leq \delta_s \leq 1.9$) suggest this time that the Kapitza instability mode is dominant.

The asymmetry between the front and back of the waves increases with the fiber radius. At $R=0.2$ mm, the genericity of the wave shape suggests that the waves resemble axisymmetric drops whose shape is affected by gravity, whereas at 1.5 mm, where the Kapitza instability is dominant, the steepening of the front is similar to what is observed in the planar case.[26]

The wave steepening may be quantified by defining a typical length of the front l_{front}. This may be tricky due to the possible presence of capillary ripples which are difficult to detect experimentally. Another experimental difficulty consists in the measurement of the substrate thickness. Indeed, a good resolution is needed because of the sensitivity of the reduced Reynolds number δ_s and saturation number $\beta_s^\star$ based on the substrate thickness. We therefore determine h_s and l_{front} with reference to the solutions to the WRIBL model (let us insist that numerical profiles are in remarkable agreement with experimental ones as shown in Fig. 16). Traveling-wave solutions to Eqs. (10) and (9) are limit-cycle trajectories of the corresponding three-dimensional dynamical system. Lengths of the tail and the front are therefore determined by considering the linear stability of the fixed point corresponding to the observed substrate thickness. Thus, h_s is given by the position of the fixed point in the phase space and l_{tail} and l_{front} are given by the inverse of the real part of the corresponding eigenvalues.

In Table I, wave characteristics are given for the waves represented in Fig. 17. Experimental and numerical data for the substrate thickness h_s, maximum thickness $h_{\max}$, and tail length l_{tail} are compared showing again good agreement. For $R=0.2$ mm and silicon oil v100, we note that the ratio $l_{\text{tail}}/l_{\text{front}}$ varies very little for the wave profiles presented in Fig. 17(a) in agreement with the observed superimposition of the said profiles, whereas $l_{\text{tail}}/l_{\text{front}}$ sharply increases with the substrate thickness for the other profiles.

Our experiments have evidenced a limitation of the amplitude of axisymmetric waves. Our observations seem to indicate that a breaking of the axisymmetry of the waves occurs when the amplitude $h_{\max}-h_s$ reaches $l_c/2$. Figure 19 illustrates the growth of a wave propagating along the fiber at low frequency ($R=1.5$ mm, $h_N=0.87$ mm, and $f_{\text{for}}=4$ Hz). The wave height increases until it reaches 1.6 mm. The wave is then too large and cannot be maintained by axial surface tension. It splits into two smaller waves.

2. On the velocity

An important feature of traveling waves concerns the phase velocity and its relation with the amplitude. We estimate experimentally the speed of the waves by determining the average slope of the crest lines on the spatiotemporal diagram. Figure 20 shows the variation of the velocity of the traveling waves with their frequency for the fiber of radius $R=0.475$ mm and $h_N=0.80$ mm. The velocity of the solution to the WRIBL model is in good agreement with experimental data even at low forcing frequencies where waves are solitarylike. For comparison, we have plotted the real part of the phase speed of the most spatially amplified linear perturbation (corresponding to the frequency of maximum response f_M defined in Sec. IV). Both curves present a minimum at an intermediate frequency. Nonlinearities are responsible for an elevation of the wave velocities as the

TABLE I. Comparisons of the experimental measurements of the substrate thickness h_s, maximum thickness h_{max}, and tail length l_{tail} to the data obtained by integration of the WRIBL model (10) and (9) for the waves presented in Fig. 17. The ratio l_{tail}/l_{front}, the reduced Reynolds number δ_s, and the saturation number $\beta_s^\star$ corresponding to the substrate of thickness h_s are also provided based on the numerical solutions. In the case of the two solitary waves labeled "sol," the numerical solution has been selected by adjusting the maximum height (boldface in the table).

Fluid	R (mm)	f_{for} (Hz)	h_N expt.±0.01 (mm)	h_s (mm)		h_{max} (mm)		l_{tail} (mm)		l_{tail}/l_{front} num.	δ_s num.	$\beta_s^\star$ num.
				Expt.±0.05	Num.	Expt.±0.05	Num.	Expt.±0.1	Num.			
v100	0.2	9	0.84	0.414	0.410	1.12	1.21	1.51	1.37	3.0	0.10	2.15
⋯	⋯	8	⋯	0.42	0.435	1.16	1.27	1.40	1.41	3.3	0.13	2.06
⋯	⋯	6	⋯	0.47	0.49	1.28	1.40	1.64	1.52	4.0	0.22	1.88
⋯	⋯	Sol	Sol	0.54	0.54	**1.54**	**1.54**	1.53	1.63	3.0	0.35	1.7
v50	0.475	7	0.62	0.4	0.41	0.925	0.91	1.55	1.41	1.9	0.22	1.1
⋯	⋯	⋯	0.76	0.54	0.51	1.325	1.30	1.95	1.7	3.2	0.55	0.99
⋯	⋯	⋯	0.86	0.61	0.56	1.7	1.64	2.5	2.0	4.9	0.85	0.94
v50	1.5	10	0.87	0.66	0.63	1.17	1.18	2.9	2.1	2.6	0.82	0.26
⋯	⋯	4	0.87	0.7	0.69	1.7	1.68	2.4	2.3	4.2	1.1	0.26
⋯	⋯	sol	sol	0.95	0.78	**2.66**	**2.66**	3.85	3.9	11	1.9	0.25

frequency is decreased from the cut-off frequency f_c. Similar trends have been observed for the two other tested fibers (R=0.2 and 1.5 mm).

In Fig. 21(a), speed and maximum thickness of solitary-like traveling waves have been normalized with reference to the speed and thickness of the Nusselt solution u_N and h_N. For a given flow rate, i.e., a given Nusselt thickness, c/u_N varies linearly with h_{max}/h_N. A fit of the experimental data gives

$$\frac{c}{u_N} \approx a\frac{h_{max}}{h_N} - b, \tag{12}$$

where the slope a is close to 1.5 and b is a constant close to unity (b=0.82, 1, and 1.3).

No correlation is observed between data corresponding to different Nusselt thicknesses when speed and maximum thickness are made dimensionless using u_N and h_N, indicating that they do not represent the correct scales. A correlation has been found, however [see Fig. 21(b)], when the velocity scale and length scale are defined with respect to the substrate of thickness h_s on which the waves propagate and to the corresponding kinematic wave speed c_{ks}. (We recall from Sec. II C that the speed of kinematic waves is equal to two times the fluid velocity at the free surface.) All experimental data then fall on a unique curve, in line with the experimental study by Tihon *et al.*[25] of solitary waves on films falling on inclined planes. This suggests that traveling waves are characterized not by the Nusselt thickness but rather by the substrate thickness on which they ride.

Figure 21(b) is completed by the amplitude-to-speed relation corresponding to the solitary-wave solutions to the WRIBL model. Comparisons to the experimental data show again a good agreement. As for solitary waves running down an inclined plane,[25] the dimensionless amplitude h_{max}/h_s and the dimensionless speed c/c_{ks} follow a linear rule,

$$\frac{c}{c_{ks}} \approx \frac{h_{max}}{h_s}. \tag{13}$$

Equation (13) corresponds to the amplitude-speed correlation obtained by Chang[27] using a normal form analysis of

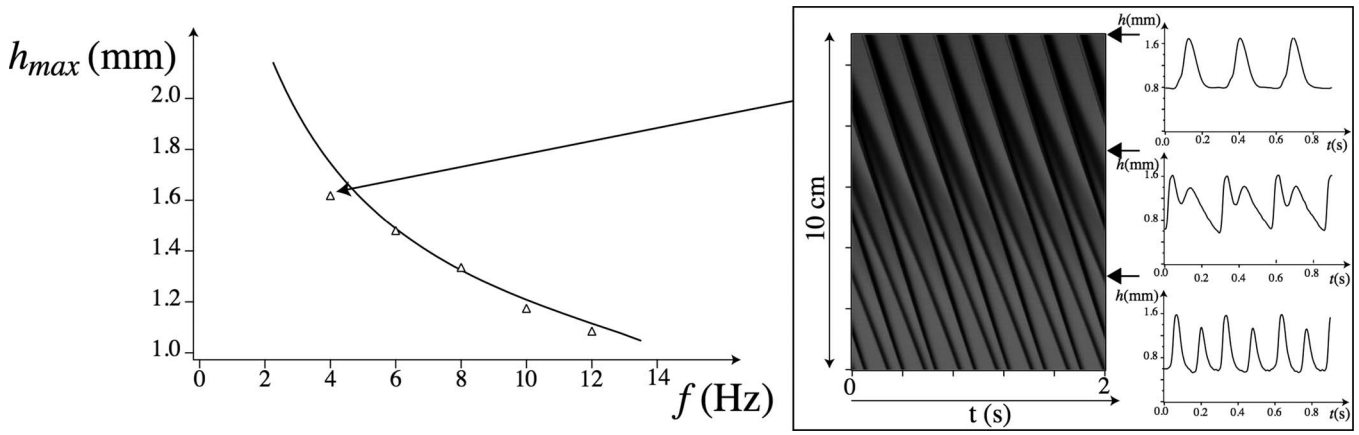

FIG. 19. R=1.5 mm and h_N=0.87 mm. Left: maximum amplitude h_{max} vs forcing frequency f_{for}. Right: Spatiotemporal diagram and times series (the locations at which the time series are taken are indicated by arrows) corresponding to the frequency f_{for}=4 Hz below which the flow starts to depart from the axisymmetric situation.

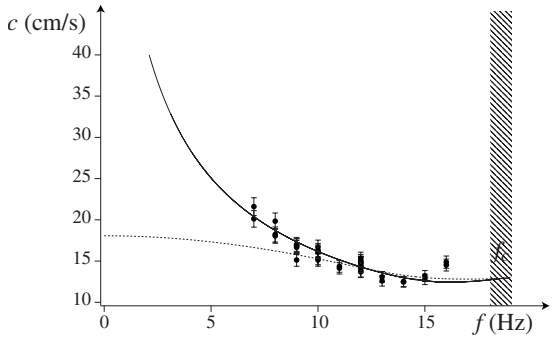

FIG. 20. Speed of the traveling waves vs frequency. Experimental data (points) are compared to the solutions to the WRIBL model (plain line). The real part of the phase speed of the linearly most amplified perturbation is indicated by a dashed line. The hatched region figures the experimental uncertainty of the cut-off frequency determination. $R=0.475$ mm and $h_N=0.80$ mm.

traveling-wave solutions to the Kuramoto–Sivashinsky equation. Since the Kuramoto–Sivashinsky equation is obtained from a weakly nonlinear analysis when viscous dispersion is negligible, the linear amplitude-speed correlation is valid only for waves of small amplitude and large Kapitza numbers, hence small $\eta=(h_N/l_c)^{4/3}$. Yet, comparisons to our experimental data as well as to corresponding data in the planar geometry show good agreement for large-amplitude waves[28] and relatively small Kapitza numbers, even if this agreement has no theoretical basis.

3. On the inner velocity distribution

Let us now consider the velocity distribution across the film corresponding to traveling waves. To have access to the flow circulation inside a bead, we have computed the streamlines in the comoving frame from the traveling-wave solutions of the WRIBL model. Four different cases are presented in Fig. 22 for the three tested fiber radii. The experimental views achieved with the high-speed camera are presented for comparison.

Numerical profiles and wavelengths are again in remarkable agreement to the experimental data which gives us confidence that the assumptions on the velocity distribution across the film sustaining the derivation of the WRIBL model are reasonable. In panel (c) the fluid moves underneath the beads and does not stagnate in them. In panels (a), (b), and (d) recirculation regions are observed, the fluid being partly trapped in the beads, which is a clear indication of carrying of mass. At $R=0.2$ mm [panel (a)], beads are separated by relatively thin films and most of the mass is carried by the beads which look like drops sliding on a quasistatic substrate.

In Ref. 8, the streamlines in the comoving frame have been reported for the traveling waves observed by Kliakhandler *et al.*[5] down a fiber with a four times more viscous fluid (Castor oil $\nu=440$ mm^2/s, $\gamma=31$ mN/m, $\rho=961$ kg/m^3, and a fiber of radius $R=0.25$ mm) where inertia is clearly negligible. Recirculation zones have also been found. The shape and flow patterns reported in panels (a) and (b) of Fig. 22 are very similar to the corresponding panels (c) and (a) of Fig. 8 in Ref. 8 even though the values of the reduced Reynolds number δ suggest that inertia is not negligible in our experiments. The ratios of the maximum thickness $h_{\max}$ and wave speed c to the substrate thickness h_s and to the speed c_{ks} of kinematic waves running on the substrate are reported in Table II. Values of $h_{\max}/h_s$ and c/c_{ks} corresponding to panels (c) and (a) of Fig. 8 in Ref. 8 and to panels (a) and (b) of Fig. 22 are indeed close, which again stresses the similarities between our results and the ones reported by Kliakhandler *et al.* for negligible inertia effects. This agreement suggests that the experiments reported in Figs. 22(a) and 22(b) belong to the droplike regime where the Rayleigh–Plateau instability dominates over the Kapitza instability. Table II has been completed with the values of the parameters based on the substrate thickness for the waves shown in Fig. 22 and in Ref. 5. The smallness of δ_s for our experiments and the good agreement of the values of $\beta_s^\star$ in our experiments and in the experiments by Kliakhandler *et al.* demonstrate again that the substrate thickness h_s is the length of reference for the description of nonlinear traveling-wave solutions and that the parameters based on the substrate flow are the ones that enable to discriminate the different regimes.

Figure 22(d) shows the inner flow pattern for the large-amplitude solitary wave presented in Fig. 7. Corresponding substrate parameters $\delta_S=1.9$ and $\beta_s^\star=0.25$ seem to indicate a prevalence of the Kapitza instability. A recirculation region is

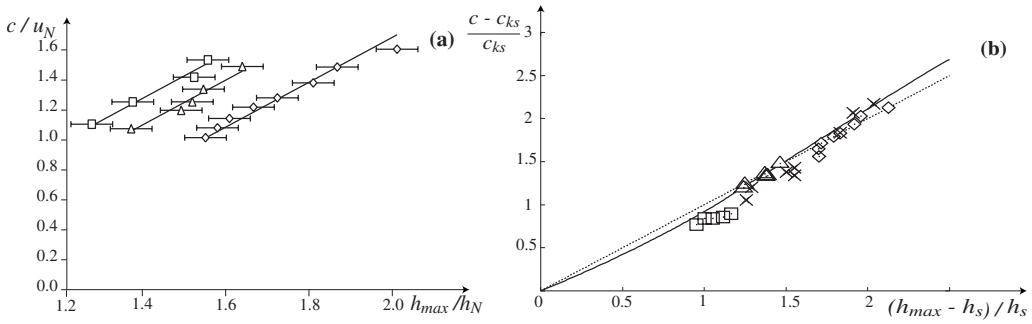

FIG. 21. (a) Dimensionless wave velocity c/u_N with the dimensionless maximum thickness $h_{\max}/h_N$. Silicon oil v50 and fiber radius $R=0.475$ mm. □: $h_N=0.61$ mm; △: $h_N=0.76$ mm; ◇: $h_N=0.87$ mm. Plain lines are linear fits. (b) $(c-c_{ks})/c_{ks}$ vs the dimensionless amplitude $(h_{\max}-h_s)/h_s$. Symbols □, △, and ◇ refer to the experimental data presented in panel (a). Crosses correspond to traveling waves obtained at $f_{\text{for}}=7$ Hz and different flow rates. Solitary-wave solutions to the WRIBL model (10) and (9) are denoted by a plain line. The dashed line is the linear approximation (13).

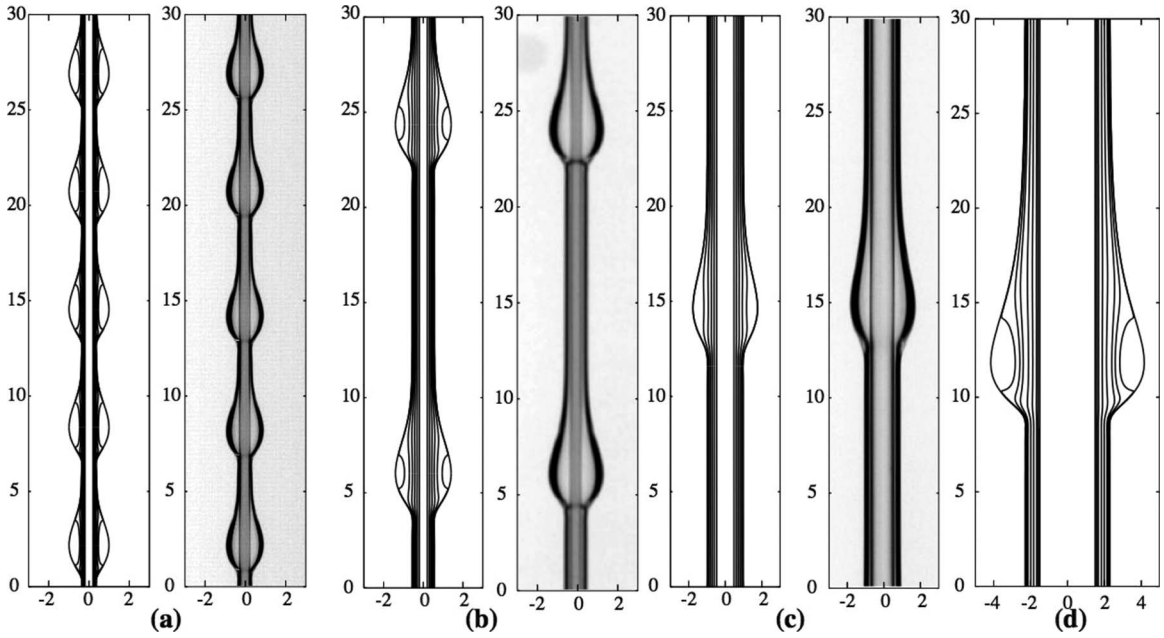

FIG. 22. Streamlines in the comoving frame from the solutions to the WRIBL model and experimental snapshots: (a) silicon oil v100, $R=0.2$ mm, $h_N=0.52$ mm, and $f=4$ Hz; (b) silicon oil v50, $R=0.2$ mm, $h_N=0.64$ mm, and $f_{\text{for}}=8$ Hz; (c) v50, $R=0.475$ mm, $h_N=0.76$ mm, and $f_{\text{for}}=7$ Hz; (d) v50, $R=1.5$ mm, and solitary wave with $h_{\max}=2.66$ mm.

also observed as expected from direct numerical simulations of large-amplitude waves in the planar geometry.[29]

Computations of the inner flow pattern for the waves observed on the fibers of radii $R=0.475$ and 1.5 mm scarcely reveal recirculation zones and only for the largest obtained solitary waves. Figure 22(c) is representative of the flow pattern usually observed. We note that the values of δ_s and $\beta_s^\star$ are then inferior to 1 and that the ratios of c/c_{ks} and $h_{\max}/h_s$ are relatively small, which suggests that the wavelike bead of moderate amplitude presented in Fig. 22(c) belongs to the drag-gravity regime.

Figure 23 and Table III compare the results obtained with the inertialess CM equation (11) to the experimental data and to the solutions to the WRIBL model. As expected, in the droplike regime [panel (a)] the CM equation provides a good estimate of the contour, amplitude, and speed of the waves. A fair agreement is obtained for larger flow rates [panel (b)]. Nevertheless, the speed of the drops (hence the wavelength) is slightly overestimated: the viscous dispersion (which is neglected in the CM model) starts to play a role, slowing down the beads. In the wavelike regime [panel (c)] the discrepancy between the experiments and the solutions to the CM model is even more noticeable due to significant inertial effects. Besides, the CM equation fails to reproduce the large-amplitude solitary waves observed in Figs. 7(b) and 22(d). In that case the instability is triggered by inertia and curvature effects are negligible, so that the solution to the CM equation has a very small amplitude (only 8% of the substrate thickness). These comparisons thus motivate the use of the WRIBL model that take into account both viscous dispersion and inertia in the wavelike regime.

TABLE II. Speed, amplitude, and parameters for the numerical solutions to the WRIBL model corresponding to Fig. 22 and to Fig. 1 in Ref. 5.

	$h_{\max}/h_s$	c/c_{ks}	δ	$\beta^\star$	δ_s	$\beta_s^\star$
Reference 5a	3.1	5.0	0.05	1.56	4×10^{-3}	2.42
Reference 5b	4.9	7.71	0.02	1.80	2×10^{-4}	3.43
Figure 22(a)	4.5	6.7	0.30	1.78	3×10^{-3}	3.36
Figure 22(b)	3.4	4.17	4.0	1.40	0.2	2.36
Figure 22(c)	2.6	2.6	3.2	0.8	0.5	0.99
Figure 22(d)	3.4	3.2	⋯	⋯	1.9	0.25

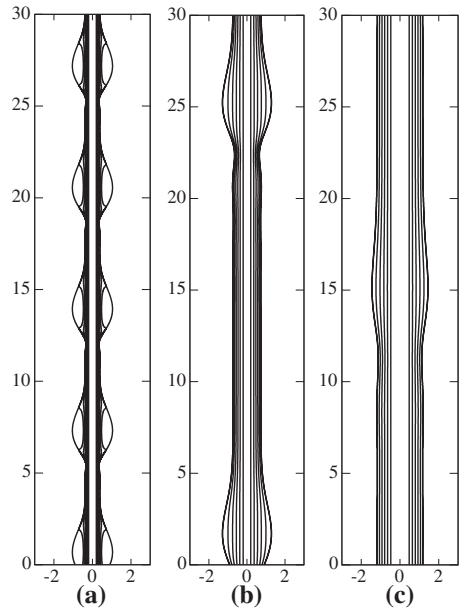

FIG. 23. Streamlines in the comoving frame from the solutions to the CM equation, corresponding to Fig. 22 panels (a)–(c).

TABLE III. Speed c (in mm/s) and amplitude h (in mm) of the waves presented in Figs. 22 and 23: experimental values and numerical solutions to the WRIBL model and to the CM equation.

Figures 22 and 23	c_{expt}	h_{expt}	c_{WRIBL}	h_{WRIBL}	c_{CM}	h_{CM}
(a)	28 ± 4	0.75 ± 0.05	24.7	0.79	26.5	0.84
(b)	150 ± 8	1.2 ± 0.1	156	1.17	188	1.09
(c)	160 ± 8	1.3 ± 0.1	171	1.16	180	0.870

VI. SUMMARY AND CONCLUSION

The spatial response of a film flowing down a fiber to inlet periodic disturbances is investigated experimentally and numerically. We scrutinize the synchronization process of the flow dynamics to the inlet forcing frequency for a convectively unstable uniform film when inertia and surface tension are equally important. Depending on the ratio of the forcing frequency to the frequency of maximum response f_{for}/f_M different scenarios have been identified. For $f_{for}\approx f_M$, the film directly responds at the forcing frequency, whereas at $f_{for}<f_M$ the formation of saturated traveling waves at the downstream end of the fiber is preceded by two or three coalescence events occurring at fixed locations on the fiber.

The shape, speed, and inner flow patterns of resulting traveling waves have been characterized for the different regimes observable on the fiber. In agreement with a recent study by Tihon *et al.* on inclined films,[25] we observe that the relevant reference scales to normalize the speed and amplitude of the beads are the speed and thickness of the uniform film of substrate thickness. The wave shape has been characterized by computing the tail and front lengths. In the droplike regime, where the Rayleigh–Plateau instability dominates over the Kapitza one, wave profiles tend to be superimposed after normalization using the amplitude and tail length of the waves. Inner flow patterns show the onset of large recirculation regions in the beads.

In the wavelike regime, where the Kapitza instability mechanism is important, a sharpening of wave fronts is observed with an increment of the flow rate or a decrement of the frequency. In most cases, recirculation zones have not been noted, the waves propagating without carrying mass. Nevertheless, for the largest observed solitary waves, a recirculation zone is again noticed. It is likely that the onset of recirculation zones in the wavelike regime is a manifestation of the transition from the drag-gravity to the drag-inertia regime. However, experimental limitations prevent us from exploring large values of δ, hence far in the drag-inertia regime.

From our results, the pertinent parameters that discriminate between the droplike and the wavelike regimes are δ_s and $\beta_s^\star$ based on the substrate flow. For that reason, the tentative flow regime diagram presented in Fig. 8 gives a first indication but must be completed. At least one more parameter, the forcing frequency, is necessary to account for the selection of the substrate thickness by the flow.

Comparisons to the solutions of a WRIBL model derived in Ref. 8 show remarkable agreement which gives us confidence in the reliability of this model even when inertia effects become dominant. From the solutions to the WRIBL model, the dispersion effects of streamwise viscous diffusion have been evidenced.[8] In particular, dispersion plays a crucial role in the selection mechanism of the natural dynamics of the film. Axisymmetric film flows down a fiber represent a prototype of active and dispersive one-dimensional medium. Such a medium is characterized by the onset of coherent structures (in our case solitary waves) generated by an instability mechanism whose one-to-one interaction is then affected by dispersion. The resulting dynamics is weakly chaotic and can be described in terms of coherent-structures interaction.[30,31] Having characterized the traveling waves in our system, we are now in a position to study wave-to-wave interactions experimentally, which is the next step in order to develop a coherent-structure theory able to describe the natural dynamics of film flows down a fiber.

ACKNOWLEDGMENTS

We thank P. Jenffer and G. Marteau for technical assistance and J. P. Hulin and S. Kalliadasis for warm and fruitful discussions.

APPENDIX: COEFFICIENT OF THE AVERAGED MOMENTUM EQUATION (9)

The coefficients of the first-order inertial terms in the momentum balance (9) consist of ratios of polynomials in b and $\log(b)$ where $b=1+\alpha h$:

$$\phi=\{3[(4\log(b)-3)b^4+4b^2-1]\}/[16(b-1)^3],$$

$$F=3F_a/[16(b-1)^2\phi F_b],$$

$$F_a=-301b^8+622b^6-441b^4+4\log(b)\times\{197b^6-234b^4+6\log(b)[16\log(b)b^4-36b^4+22b^2+3]b^2+78b^2+4\}b^2+130b^2-10,$$

$$F_b=17b^6+12\log(b)[2\log(b)b^2-3b^2+2]b^4-30b^4+15b^2-2,$$

$$G=G_a/[64(b-1)^4\phi^2F_b],$$

$$\{G_a=9b\{4\log(b)[-220b^8+456b^6-303b^4+6\log(b)\times(61b^6-69b^4+4\log(b)(4\log(b)b^4-12b^4+7b^2+2)b^2+9b^2+9)b^2+58b^2+9]\,b^2+(b^2-1)^2(153b^6-145b^4+53b^2-1)\},$$

$$I=64(b-1)^5\phi^2/[3F_b].$$

The coefficients of the second-order streamwise viscous terms in Eq. (9) read

$$J = J_a/[128(b-1)^4\phi^2 F_b],$$

$$J_a = 9\{(490b^8 - 205b^6 - 235b^4 + 73b^2 - 3)(b^2-1)^3 + 4b^2\log(b)[2b^4\log(b)(72\log(b)(2\log(b)b^4 - 6b^4 + b^2 + 6)b^4 + (b-1)(b+1)(533b^6 - 109b^4 - 451b^2 + 15)) - 3(b^2-1)^2(187b^8 - 43b^6 - 134b^4 + 17b^2 + 1)]\},$$

$$K = 3K_a/[16b^3(b-1)^2\phi F_b],$$

$$K_a = 4b^4\log(b)(233b^8 - 360b^6 + 12\log(b)(12\log(b)b^4 - 25b^4 + 12b^2 + 9)b^4 + 54b^4 + 88b^2 - 15) - (b^2-1)^2(211b^8 - 134b^6 - 56b^4 + 30b^2 - 3),$$

$$L = L_a/[8b(b-1)^2\phi F_b],$$

$$L_a = 4b^2\log(b)\{6\log(b)(12\log(b)b^4 - 23b^4 + 18b^2 + 3)b^4 + (b-1)(b+1)(95b^6 - 79b^4 - 7b^2 + 3)\} - (b^2-1)^2(82b^6 - 77b^4 + 4b^2 + 3),$$

$$M = 3 + [24\log(b)b^8 - 25b^8 + 48b^6 - 36b^4 + 16b^2 - 3]/[2b^2F_b].$$

[1] P. L. Kapitza, in *Collected Papers of P. L. Kapitza*, edited by D. Ter Haar (Pergamon, New York, 1965), pp. 662–689.
[2] P. L. Kapitza and S. P. Kapitza, in *Collected Papers of P. L. Kapitza*, edited by D. Ter Haar (Pergamon, New York, 1965), pp. 690–709.
[3] D. Quéré, "Thin films flowing on vertical fibers," Europhys. Lett. **13**, 721 (1990).
[4] D. Quéré, "Fluid coating on a fiber," Annu. Rev. Fluid Mech. **31**, 347 (1999).
[5] I. L. Kliakhandler, S. H. Davis, and S. G. Bankoff, "Viscous beads on vertical fibre," J. Fluid Mech. **429**, 381 (2001).
[6] R. V. Craster and O. K. Matar, "On viscous beads flowing down a vertical fibre," J. Fluid Mech. **553**, 85 (2006).
[7] C. Duprat, C. Ruyer-Quil, S. Kalliadasis, and F. Giorgiutti-Dauphiné, "Absolute and convective instabilities of a film flowing down a vertical fiber," Phys. Rev. Lett. **98**, 244502 (2007).
[8] C. Ruyer-Quil, P. Treveleyan, F. Giorgiutti-Dauphiné, C. Duprat, and S. Kalliadasis, "Modelling film flows down a fibre," J. Fluid Mech. **603**, 431 (2008).
[9] H.-C. Chang and E. A. Demekhin, *Complex Wave Dynamics on Thin Films* (Elsevier, Amsterdam, 2002).
[10] V. Ya. Shkadov, "Solitary waves in a layer of viscous liquid," Izv. Akad. Nauk SSSR, Mekh. Zhidk. Gaza **1**, 63 (1977).
[11] G. M. Sisoev, R. V. Craster, O. K. Matar, and S. V. Gerasimov, "Film flow down a fibre at moderate flow rates," Chem. Eng. Sci. **61**, 7279 (2006).
[12] S. Kalliadasis and H.-C. Chang, "Drop formation during coating of vertical fibres," J. Fluid Mech. **261**, 135 (1994).
[13] O. Takeshi, "Surface equation of falling film flows with moderate Reynolds number and large but finite Weber number," Phys. Fluids **11**, 3247 (1999).
[14] C. Ruyer-Quil and P. Manneville, "On the speed of solitary waves running down a vertical wall," J. Fluid Mech. **531**, 181 (2005).
[15] L. Brevdo, F. Dias, T. J. Bridges, and P. Laure, "Convective unstable wave packets in a film flow down an inclined plane," J. Fluid Mech. **396**, 37 (1999).
[16] A. L. Frenkel, "Nonlinear theory of strongly undulating thin films flowing down vertical cylinders," Europhys. Lett. **18**, 583 (1992).
[17] Yu. Ya Trifonov, "Steady-state travelling waves on the surface of a viscous liquid film falling down vertucal wires and tubes," AIChE J. **38**, 821 (1992).
[18] V. Ya. Shkadov, "Wave flow regimes of a thin layer of viscous fluid subject to gravity," Izv. Akad. Nauk SSSR, Mekh. Zhidk. Gaza **1**, 43 (1967).
[19] C. Ruyer-Quil and P. Manneville, "Improved modeling of flows down inclined planes," Eur. Phys. J. B **15**, 357 (2000).
[20] A. Oron, O. Gottlieb, and E. Novbari, "Numerical analysis of a weighted-residual integral boundary-layer model for nonlinear dynamics of falling liquid films," Eur. J. Mech. B/Fluids **28**, 1 (2009).
[21] F. J. Solorio and M. Sen, "Linear stability of a cylindrical falling film," J. Fluid Mech. **183**, 365 (1987).
[22] E. J. Doedel, AUTO07P, continuation and bifurcation software for ordinary differential equations, Montreal Concordia University, 2008.
[23] S. V. Alekseenko, V. Y. Nakoryakov, and B. G. Pokusaev, "Wave formation on a vertical falling liquid film," AIChE J. **31**, 1446 (1985).
[24] J. Liu and J. P. Gollub, "Solitary wave dynamics of film flows," Phys. Fluids **6**, 1702 (1994).
[25] J. Tihon, K. Serifi, K. Argyriadi, and V. Bontozoglou, "Solitary waves on inclined films: Their characteristics and the effects on wall shear stress," Exp. Fluids **41**, 79 (2006).
[26] S. V. Alekseenko, V. E. Nakoryakov, and B. G. Pokusaev, *Wave Flow in Liquid Films* (Begell, New York, 1994).
[27] H.-C. Chang, "Traveling waves on fluid interfaces: Normal form analysis of the Kuramoto-Sivashinsky equation," Phys. Fluids **29**, 3142 (1986).
[28] H.-C. Chang, "Wave evolution on a falling film," Annu. Rev. Fluid Mech. **26**, 103 (1994).
[29] P. N. Yoshimura, T. Nosoko, and T. Nagata, "Enhancement of mass transfer into a falling laminar liquid film by two-dimensional surface waves—some experimental observations and modeling," Chem. Eng. Sci. **51**, 1231 (1996).
[30] N. J. Balmforth, G. R. Ierley, and E. A. Spiegel, "Chaotic pulse trains," SIAM J. Appl. Math. **54**, 1291 (1994).
[31] N. J. Balmforth, "Solitary waves and homoclinic orbits," Annu. Rev. Fluid Mech. **27**, 335 (1995).